An investigation of the strain dependence of dynamic precipitation in an Al-Zn-Mg-Cu alloy

L. Couturier, A. Deschamps, Frédéric de Geuser, F. Fazeli, W.J. Poole

An investigation of the strain dependence of dynamic precipitation in an Al-Zn-Mg-Cu alloy

L. Couturier[a,b], A. Deschamps[c], F. De Geuser[c], F. Fazeli[d], W.J. Poole[a]

[a]Departement of Materials Engineering, The University of British Columbia, Vancouver, B.C., V6T 1Z4, Canada
[b]Institut des Matériaux Jean Rouxel (IMN), Université de Nantes, CNRS, 2 rue de la Houssinières, BP 32229, 44322 Nantes Cedex 3, France
[c]Univ. Grenoble Alpes, CNRS, Grenoble INP, SIMaP, F-38000 Grenoble, France
[d]CanmetMATERIALS, Natural Resources Canada, Hamilton, ON, L8P 0A5, Canada

Corresponding author: L. Couturier, laurent.couturier55@hotmail.fr, Rue Christian Pauc BP50609, 44306 Nantes Cedex 3, France.

Abstract

The use of high strength Al-Zn-Mg-Cu alloys in automotive components is restricted by their low formability. Warm forming in the under-aged state improves formability, but induces a strain-dependent microstructure evolution due to dynamic precipitation. We present a new methodology to quantitatively evaluate the dynamic precipitation strain dependence which is applicable to strain rates relevant to forming. The plastic strain is varied using a tapered tensile sample and the precipitation state is measured in terms of size and volume fraction using spatially resolved small-angle X-ray scattering, showing its evolution during straining is dependent on the imposed strain level and rate.

Keywords: aluminum alloys, precipitation, dynamic phenomena, small angle X-ray scattering (SAXS)

Aluminium alloys from the 7xxx series (Al-Zn-Mg-Cu) are traditionally used in aerospace components due to their high level of yield strength [1,2]. This strength is related to a precipitation sequence which involves clustering and the formation of GP zones at room temperature, followed by transformation to the metastable η' phase at the peak strength and finally the transformation to the η phase during over-ageing [3–6]. The use of these alloys is also of interest for automotive applications where high strength alloys could lead to significant weight savings which is a viable strategy to reduce the environmental impact of automobiles while maintaining crash worthiness [7,8]. However, the use of 7xxx alloys in automotive components is restricted by their low formability in the T6 temper at ambient temperature [9–11]. In order to overcome that limitation, warm forming of alloys such as 7020, 7150, 7921 and 7075 alloys has been investigated and proven to enhance their formability [9–16]. In particular, some of these studies reported that the formability of 7075 alloy in the T6 condition is significantly improved around 200°C [9,11,12]. Only recently has there been some attention on the consequences of warm forming on the materials hardening phases and therefore on the final properties of the formed parts [10,11,14–16]. In order to benefit from improved ductility during forming without a loss of the material strength in the final part, recent research has proposed warm forming in the underaged state of these alloys [10]. This opens the possibility for dynamic precipitation which has previously been shown to occur in the 7XXX aluminum alloy series [17–19]. Dynamic precipitation during warm forming could be used to transform

an underaged material to its peak strength concurrent with the forming. However, one of critical issues would be the effect of strain on dynamic precipitation [20–22], i.e. during forming of actual part, there would be wide range of local strains and strain rates. This is important since this inhomogeneity of strain and resulting effect on dynamic precipitation would translate to inhomogeneous properties in the final product.

Previous studies have shown that small angle X-ray scattering (SAXS) has the capability to accurately quantify the state of precipitation in 7xxx alloys. Thus, it is proposed that SAXS is a promising technique to evaluate the influence of initial microstructure, strain and strain rate, and deformation temperature [19–21] on the characteristics of dynamic precipitation. For example, SAXS studies have shown that deformation accelerates the precipitation of GP zones at room temperature [17,19] and the growth and coarsening of precipitates during artificial ageing [21]. The role of strain-induced excess vacancies has been proposed to explain the strain rate dependence of dynamic precipitation during monotonic straining at artificial ageing temperatures [21] as well as during room temperature cyclic straining [19]. The introduction of *in-situ* tensile SAXS experiments during the 2000's [17,20] introduced a technique to follow the evolution of precipitate characteristics during deformation and therefore to evaluate precisely the strain-dependence of this process. However, such *in-situ* experiments are restricted to relatively low strain rates (≈10^{-3} s^{-1}), which are unrealistic for the application to warm forming of automotive components where strain rates are several orders of magnitude higher (≈0.1-10 s^{-1}). In this paper, we present a new methodology to analyze the strain dependence of dynamic precipitation to high strain rates. The strain level was continuously varied on a single tapered tensile sample, and the post-straining precipitation state was quantitatively evaluated using spatially-resolved small-angle X-ray scattering. These SAXS experiments permit a better understanding of the interplay between forming parameters, microstructure and properties of the warm formed products.

In the current work, the aluminum alloy 7068 was studied, (composition is given in **Table 1**). Axisymmetric tapered tensile samples (**Figure 1**) were machined from a 10 mm thick hot rolled plate. The samples had a symmetric gauge section whose diameter varied from 4.674 mm to 3.8 mm with a radius of curvature equal to 280 mm. The heat treatment of the samples involved a solution treatment at 753 K for 3.6 ks, followed by water quenching and then an artificial ageing step of 5.4 ks at 378 K to produce an underaged precipitation state. These tensile samples were loaded in the servo-hydraulic test frame (MTS 810 load frame), were heated to the test temperature of 448 K at constant heating rate of 0.4 K/s, while the whole test set-up (tensile grips and specimen) was surrounded by insulation to ensure the test temperature homogeneity and stability during the experiment. Deformation at two different stroke rates (0.02 and 20 mm/s) was commenced as soon as the test temperature was reached with the maximum plastic strain reaching 0.145 and 0.181, respectively. After the test, the sample was immediately air quenched to room temperature (around 60 s to go from 448 K, at the end of deformation, to below 353 K). Since the specimen is not observable during deformation because of the set-up insulation, Digital Image Correlation (DIC) could not be used. Instead, a measurement of the total strain distribution along the sample axis was obtained by measuring, before and after deformation, the distances between adjacent grid points (4 lines parallel to the tensile axis all around the specimen crossed by perpendicular lines) which had been placed on the sample. Then, a 100 µm thin slice parallel to the loading axis was produced from each tensile sample for the SAXS measurements by mechanical grinding and polishing. SAXS experiments were conducted on a laboratory instrument using a rotating anode with a Cu target and a Pilatus 2D detector. The beam width on the sample, which defines the spatial resolution of the precipitate characterization along the sample, was 0.5 and 1.0 mm for the samples deformed at 0.02 and 20 mm/s, respectively. The SAXS 2D-data was radially averaged and

normalized into the 1D-profile of scattered intensity *I* versus the scattering vector amplitude *q*; detailed procedures for data interpretation can be found in reference [23].

	Mg	Zn	Cu	Cr	Zr	Fe	Si	Al
%at.	3.04	3.32	0.890	0.021	0.038	0.061	0.045	bal.
%wt.	2.59	7.61	1.98	0.039	0.12	0.12	0.044	bal.

Table 1: Chemical composition of the studied 7068 aluminum alloy.

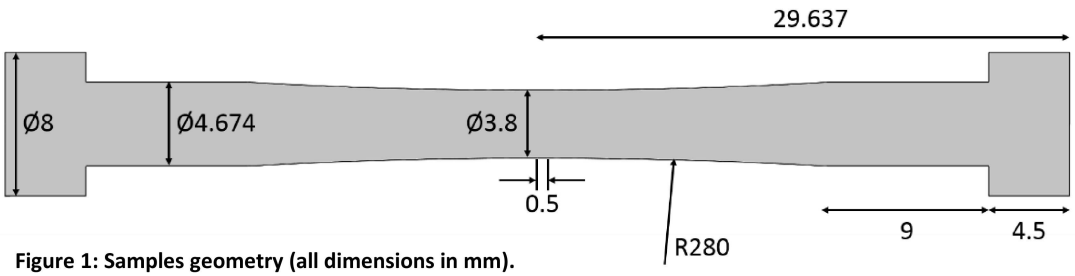

Figure 1: Samples geometry (all dimensions in mm).

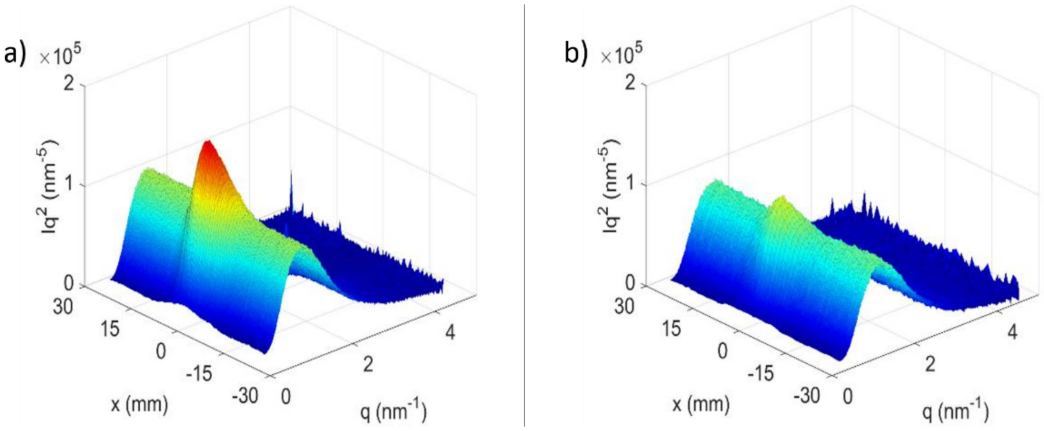

Figure 2: Evolution of the Kratky representation (Iq^2 vs. q) along the tensile axis (x) for the underaged 7068 samples deformed at 448 K at 0.02 mm.s^{-1} (a) and 20 mm.s^{-1} (b).
Note: x = 0, is the centre of the sample shown in Figure 1.

Figure *2* displays the results obtained during the SAXS experiments from the samples deformed at low and high stroke rate. These two graphs are Kratky representations of the azimuthally averaged scattered intensities measured along the samples. In this type of representation, the position of the maximum of Iq^2 for different positions along the sample gauge length (x) is inversely proportional to the average radius of the precipitates and the integrated intensity Q_0 is proportional to the precipitate volume fraction [23]. This data illustrates that plastic deformation has a strong effect on the state of precipitation since these curves are markedly different in the central region (i.e. near x =0) where the maximum level of deformation occurred, i.e. the maximum value of Iq^2 is much larger for the sample

deformed at 0.02 mm/s compared to 20 mm/s, with maximum of Iq^2 equal to $1.78x10^5$ nm^{-5} and to $1.17x10^5$ nm^{-5} respectively. Qualitatively, the general results can be deduced from the Kratky plots in Figure 2. At the ends of the samples, greater than ± 20 mm from the centre, where the diameter is the largest (4.67 mm), no plastic deformation occurs and precipitation is homogeneous as indicated by similar Kratky plots. As one moves towards the centre of the sample, the average size of the precipitates increases gradually with increasing strain level, i.e. the plastic strain increases as the diameter of the tensile sample decreases. Further, it is noted this effect is larger for the stroke rate of 0.02 mm/s compared to 20 mm/s. In the following, the Guinier radius, R_g, calculated in a self-consistent manner as described in [23] and the integrated intensity Q_0 will be used to quantify the state of precipitation. For further details regarding the analysis of precipitation state using SAXS data, the reader is referred to the corresponding literature [23–25].

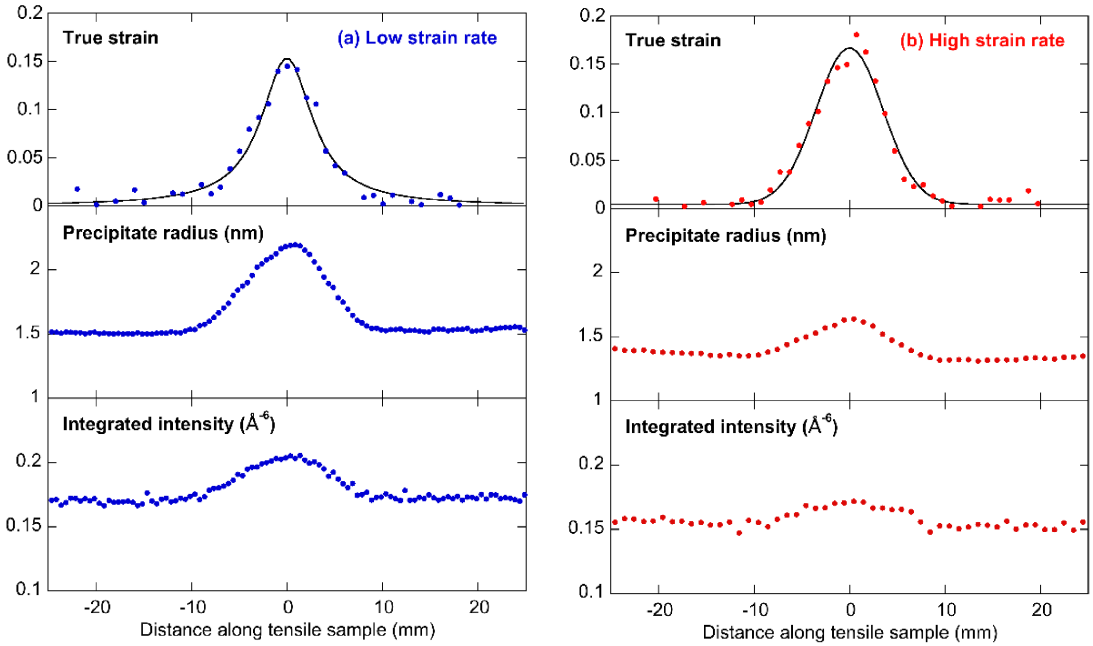

Figure 3: Evolution of the local plastic strain, precipitates' Guinier radius and integrated intensity scattered by precipitates along the tensile axis for the underaged 7068 samples deformed at 448 K at 0.02 $mm.s^{-1}$ (a) and 20 $mm.s^{-1}$ (b). The local plastic strain measurements (dots) are represented together with the fit of their evolution with distance (pseudo-Voigt function) in black.

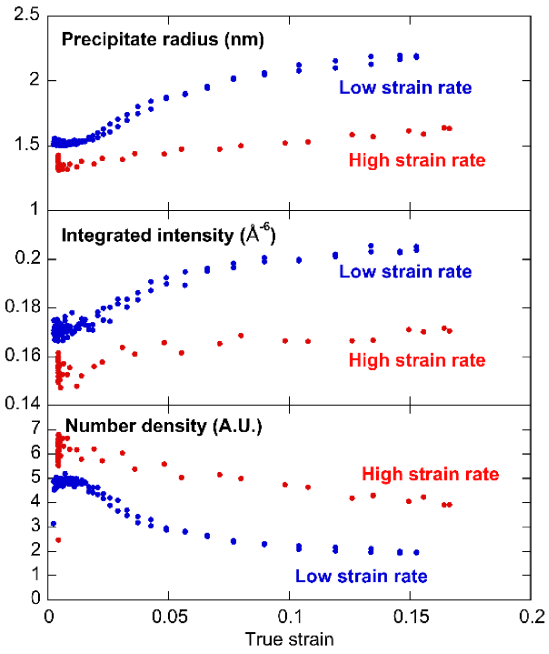

Figure 4: Evolution of the precipitates Guinier radius, the associated integrated intensity and the resulting number density of precipitates with the plastic strain for the underaged 7068 samples deformed at 448 K at 20 mm.s^{-1} (in red) and 0.02 mm.s^{-1} (in blue).

Figure *3* shows the precipitate characteristics, R_g and Q_0, and the plastic strain measurements along the length of the tensile samples for deformation conditions of 0.02 and 20 mm/s. It can be observed in the upper figure that going from left to right on the sample, the plastic strain increases from zero to a maximum of 15-20% and then decreases to zero again. This could be fit by pseudo-Voigt function [26,27]. Note, the maximum strain in the sample deformed at 20 mm/s was slightly larger than that of 0.02 mm/s, i.e. 0.181 vs 0.145, respectively. Turning to the state of precipitates, the first thing to notice is that SAXS measurements show that in the undeformed portion of the sample (i.e. greater than ±10 mm) precipitates have a slightly larger radius (1.52 vs 1.36 nm) and a slightly higher volume fraction (higher Q_0 of 1.71 vs 1.55 x10^5 nm^{-6}) for the sample deformed at 0.02 mm/s. This can be attributed to the fact that the time required to conduct the deformation (and hence the time at temperature) at this low crosshead speed was longer, i.e. the material was aged at 448 K for 73 s for the deformation at 0.02 mm/s vs < 1 s for the deformation at 20 mm/s and precipitate growth during this time would explain the difference.

Next, it can be observed that even though the maximum strain reached in the case of the deformation at 20 mm/s is slightly higher than for the case of 0.02 mm/s, the increase in the precipitate radius at the centre of the sample compared to the shoulder of the sample is only 1.32 to 1.64 nm, compared to 1.50 to 2.20 nm for the sample deformed at 0.02 mm/s. Further, the evolution of Q_0 follows the same trend. The observation that the evolution of precipitate state depends on strain rate is consistent with what was measured previously by Deschamps et al. during the deformation of a 7010 alloy, albeit at much slower strain rates, 4.10^{-3} s^{-1} and $2.10^{-4}s^{-1}$, and at room temperature [17]. To see the relationship between plastic strain and the state of precipitation derived from SAXS, the data can be cross-plotted by taking the precipitate state and the plastic strain measurement at the same spatial location in the sample (**Error! Reference source not found.**) using the pseudo-Voigt fit of the plastic strain (black line on the top graphs from **Figure 3**).

Error! Reference source not found. displays the dependence of both R_g and Q_0 with plastic strain recalling that Q_0 is proportional to the precipitate volume fraction. The robustness of the measurements can be demonstrated by noting that the measurements from either side of the sample centre give very similar results (this is most clearly seen in the pairs of data points in the high strain rate sample). These results also illustrate the strong effect of plastic strain on precipitation, with a monotonic evolution of both size and precipitate volume fraction as a function of strain. Further, it can be clearly observed that the increase in precipitate radius or volume fraction during deformation is much greater for sample deformed at a slower speed. It is worth emphasizing that this is not just an effect of extra time which, as was previously mentioned, caused a change in radius of only ≈0.1 nm compared to difference of 0.7 nm which was found in the sample deformed at 0.02 mm/s. It is also useful to consider the evolution of precipitate number density as function of plastic strain. This is shown in Figure 4 in arbitrary units and was calculated from Q_o and R_g, i.e. Q_o/R_g^3. The continuous decrease in precipitate number density during straining suggests that nucleation does not occur during these experiments, and, thus, that the main role of plastic strain is to accelerate precipitate growth and coarsening.

This observation would be consistent with the role of excess vacancies created by plastic straining on the diffusion rate of solutes [21]. A comparison of the two stroke rates shows that the rate of dynamic precipitation is strain rate dependent. Such a dependence was not observed by Fribourg et al. [20], although for lower strain rates as compared to the present study. They attributed their results to the competition between a shorter time available for dynamic precipitation and a higher rate of vacancy generation at high strain rates. On the other hand, Hutchinson et al. [19] showed a strain rate dependence in the case of low cycle fatigue, which they ascribed to the competition between vacancy generation and annihilation. Clearly the effect of strain rate on dynamic precipitation is a complex issue, which needs to be investigated in a wide range of experimental conditions.

One limitation of the methodology is the variation of strain rate along the gauge length of the sample. One cannot assess experimentally the evolution of strain rate along the sample due to the inability to view the sample during the test because of the insulation surrounding the sample. However one can compute the average strain rate at the sample centre by taking the maximum strain divided by the time of test, which yields ≈ $1.6x10^{-3}$ s^{-1} and ≈ 1.8 s^{-1} for tests done at 0.02 mm/s and 20 mm/s respectively. As one moves from the centre towards the end of the sample, the plastic strain decreases and thus, the corresponding strain rate decreases, for example, at a plastic strain of 0.05, the average strain rate for the deformation would be 0.5 s^{-1} and $5.6x10^{-4}$ s^{-1}. It is proposed that this factor of ≈ 3 decrease in strain

rate is a second order effect compared to the overall difference in strain rate of ≈ 1000 between the two test conditions.

Further, our results show a negative dependence of the dynamic precipitation kinetics to strain rate, therefore the effect of strain on dynamic precipitation demonstrated along our samples of variable section is a lower bound of the same effect that would be obtained at constant strain rate. Moreover, the situation of an imposed strain (vs. an imposed strain rate) is close to that found during metal forming.

In summary, the methodology presented in this work opens the way for an efficient characterization of the strain dependence of dynamic precipitation in aluminum 7XXX alloys over a wide range of deformation rates and deformation levels. In particular, this allows for the investigation of precipitate evolution during warm forming i.e. involving very high strain rates that cannot be achieved during in-situ experiments. The results show that even at very high strain rates, dynamic precipitation occurs in under-aged 7XXX aluminum alloys, although the observed effect is smaller than that observed at lower strain rates. This methodology opens the way for a systematic investigation of the effect of the salient parameters such as strain rate, initial temper, temperature and alloy composition on the strain dependence of dynamic precipitation and its consequences on mechanical properties.

The project is partially funded by the Government of Canada through ecoEII-TR37 grant and by the Natural Science and Engineering Research Council (NSERC) Discovery Grant.

References

[1] Starke Jr., E. A., Staley, J. T., *Prog. Aerosp. Sci.* 1996, 32, 131–172.
[2] Williams, J. C., Starke Jr., E. A., *Acta Mater.* 2003, 51, 5775–5799.
[3] Löffler, H., Kovács, I., Lendvai, J., *J. Mater. Sci.* 1983, 18, 2215–2240.
[4] Lendvai, J., *Mater. Sci. Forum* 1996, 217–222, 43–56.
[5] Li, X. Z., Hansen, V., GjØnnes, J., Wallenberg, L. R., *Acta Mater.* 1999, 47, 2651–2659.
[6] Wolverton, C., *Acta Mater.* 2001, 49, 3129–3142.
[7] Miller, W. S., Zhuang, L., Bottema, J., Wittebrood, A. J., De Smet, P., Haszler, A., Vieregge, A., *Mater. Sci. Eng. A* 2000, 280, 37–49.
[8] Hirsch, J., *Mater. Trans.* 2011, 52, 818–824.
[9] WANG, H., LUO, Y., FRIEDMAN, P., CHEN, M., GAO, L., *Trans. Nonferrous Met. Soc. China* 2012, 22, 1–7.
[10] Kumar, M., Ross, N. G., *J. Mater. Process. Technol.* 2016, 231, 189–198.
[11] Huo, W., Hou, L., Zhang, Y., Zhang, J., *Mater. Sci. Eng. A* 2016, 675, 44–54.
[12] Lee, M.-Y., Sohn, S.-M., Kang, C.-Y., Suh, D.-W., Lee, S.-Y., *J. Mater. Process. Technol.* 2004, 155–156, 1337–1343.
[13] Rokni, M. R., Zarei-Hanzaki, A., Roostaei, A. A., Abedi, H. R., *Mater. Des.* 2011, 32, 2339–2344.
[14] Kumar, M., Poletti, C., Degischer, H. P., *Mater. Sci. Eng. A* 2013, 561, 362–370.
[15] Kumar, M., Sotirov, N., Chimani, C. M., *J. Mater. Process. Technol.* 2014, 214, 1769–1776.
[16] JIANG, F., ZHANG, H., WENG, S., FU, D., *Trans. Nonferrous Met. Soc. China* 2016, 26, 51–62.
[17] Deschamps, A., Bley, F., Livet, F., Fabregue, D., David, L., *Philos. Mag.* 2003, 83, 677–692.
[18] Hörnqvist, M., Karlsson, B., *Procedia Eng.* 2010, 2, 265–273.

[19] Hutchinson, C. R., de Geuser, F., Chen, Y., Deschamps, A., *Acta Mater.* 2014, 74, 96–109.
[20] Fribourg, G., Deschamps, A., Bréchet, Y., *Proc. ICAA11* 2008, 936–946.
[21] Deschamps, A., Fribourg, G., Bréchet, Y., Chemin, J. L., Hutchinson, C. R., *Acta Mater.* 2012, 60, 1905–1916.
[22] Liu, S., Wang, S., Ye, L., Deng, Y., Zhang, X., *Mater. Sci. Eng. A* 2016, 677, 203–210.
[23] De Geuser, F., Deschamps, A., *Comptes Rendus Phys.* 2012, 13, 246–256.
[24] Deschamps, A., DeGeuser, F., *J. Appl. Crystallogr.* 2011, 44, 343–352.
[25] Glatter, O., Kratky, O., *Small Angle X-Ray Scattering*, Academic Press 1982.
[26] Wertheim, G. K., Butler, M. A., West, K. W., Buchanan, D. N. E., *Rev. Sci. Instrum.* 1974, 45, 1369–1371.
[27] Enzo, S., Fagherazzi, G., Benedetti, A., Polizzi, S., *J. Appl. Crystallogr.* 1988, 21, 536–542.

Table 1

	Mg	Zn	Cu	Cr	Zr	Fe	Si	Al
%at.	3.04	3.32	0.890	0.021	0.038	0.061	0.045	bal.
%wt.	2.59	7.61	1.98	0.039	0.12	0.12	0.044	bal.

Table 1: Chemical composition of the studied 7068 aluminum alloy.

Figure 3
Click here to download high resolution image

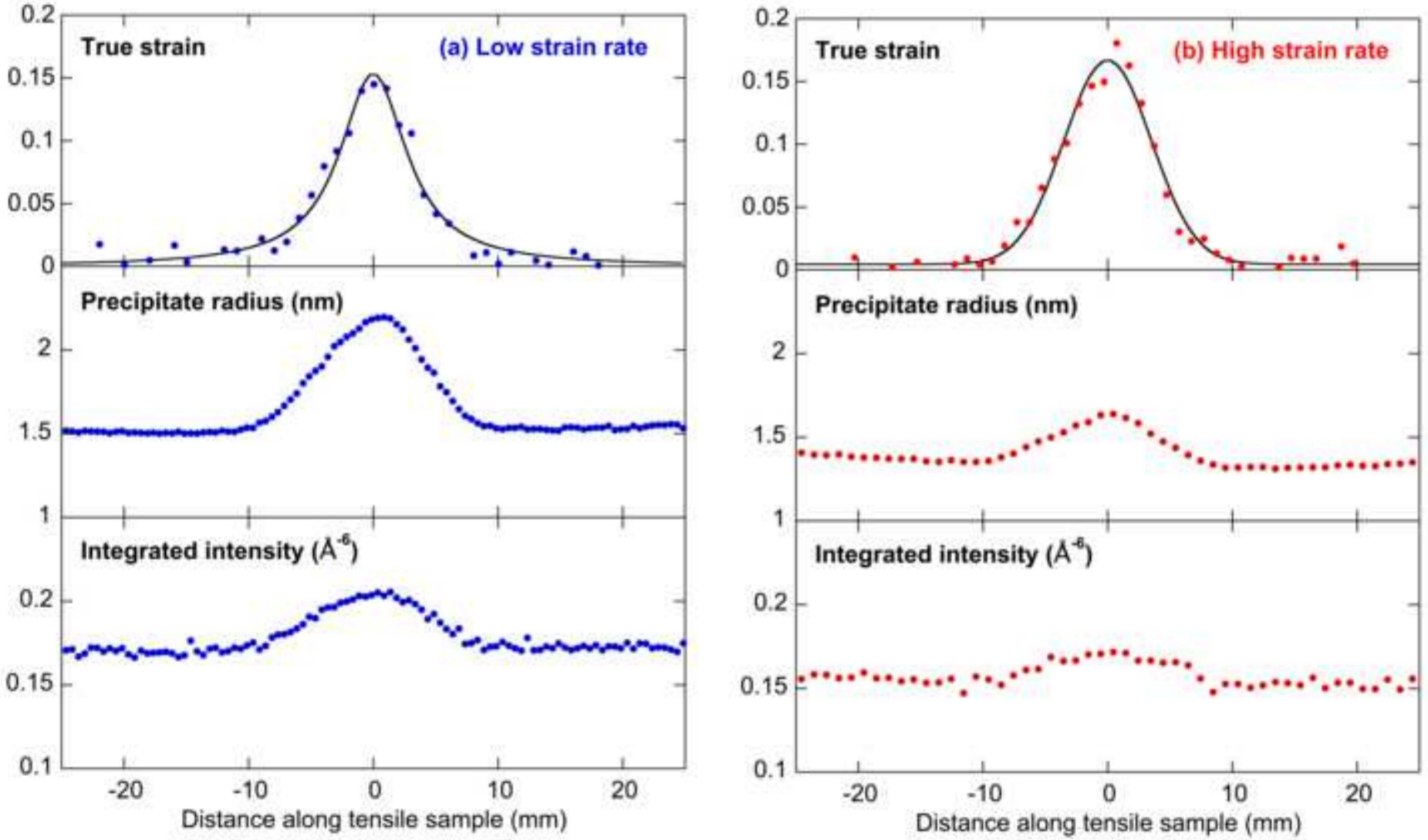

Figure 4
Click here to download high resolution image

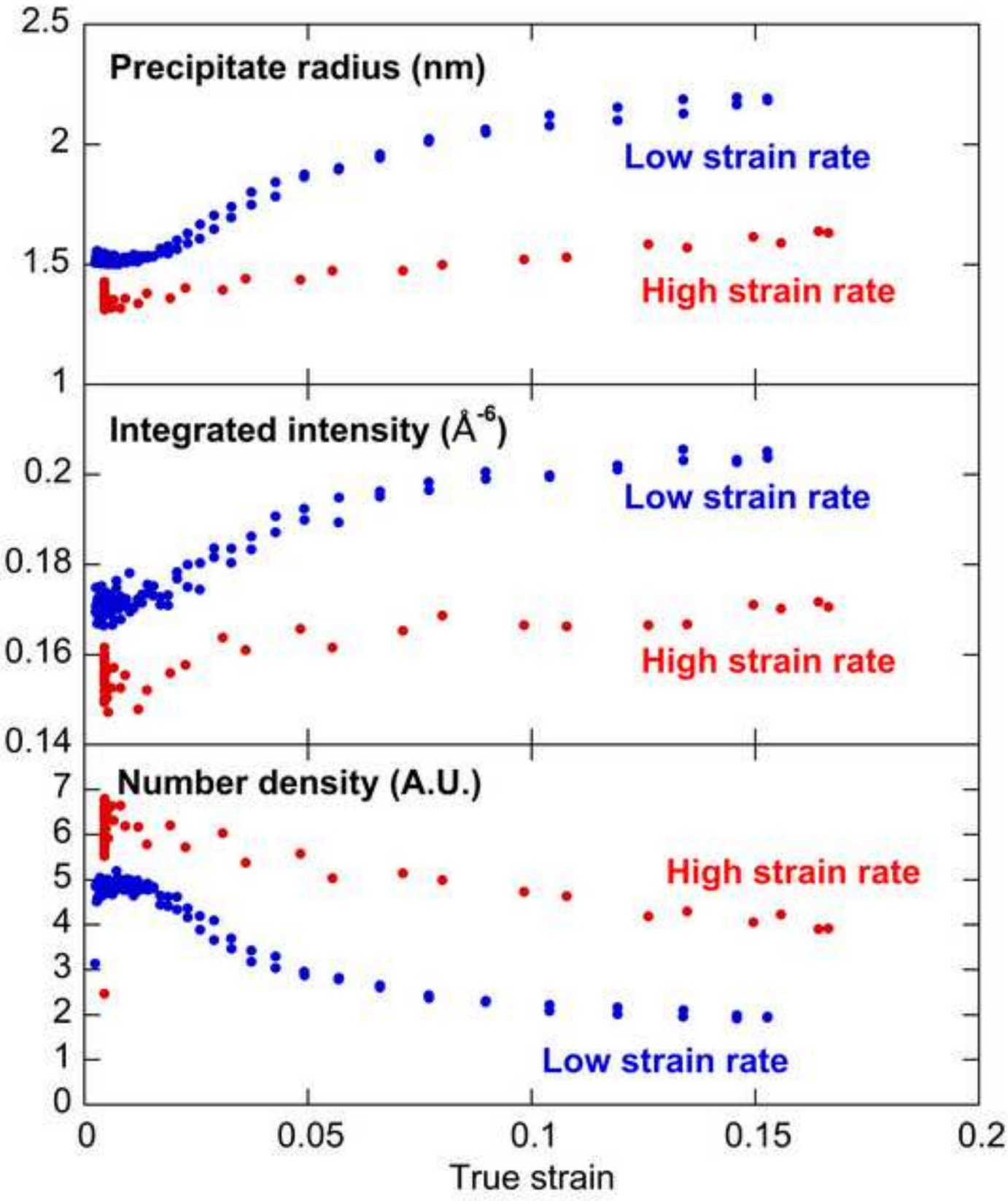

Figure 1
Click here to download high resolution image

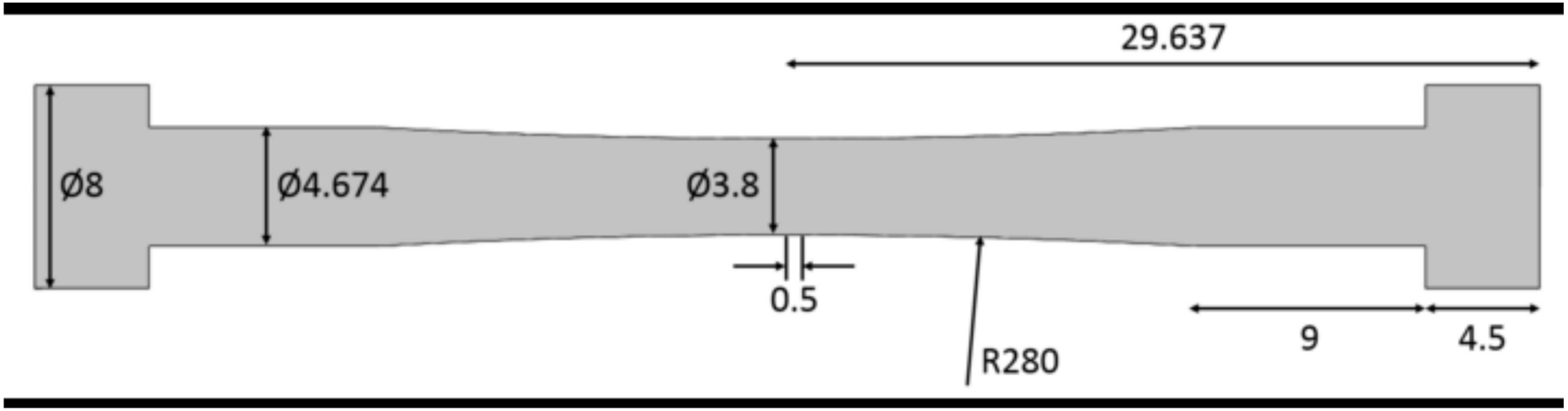

Figure 2
Click here to download high resolution image